Received: Added at production | Revised: Added at production | Accepted: Added at production

DOI: xxx/xxxx

RESEARCH ARTICLE

Sensitivity of Multiscale Large Eddy Simulations for Wind Power Production in Complex Terrain

Giorgia De Moliner[1] | **Paolo Giani**[2] | **Giovanni Lonati**[1] | **Paola Crippa**[2]

[1]Department of Civil and Environmental Engineering, Politecnico di Milano, Milan, Italy

[2]Department of Civil and Environmental Engineering and Earth Sciences, University of Notre Dame, IN, USA

Correspondence
Email: pcrippa@nd.edu ;
Email: giovanni.lonati@polimi.it

Funding Information
This research was supported by the the National Science Foundation under Grant No. 2236504 to PC

Abstract

Coupling Large Eddy Simulations (LES) with Numerical Weather Prediction (NWP) models has promising applications for wind energy. Regional climatology, optimal siting of wind turbines as well as short term wind energy forecasts can be improved by considering all the energetic scales of atmospheric motions. However, the complexity of NWP-LES coupled simulations introduces challenges and uncertainties that need to be addressed. This study focuses on understanding the relative importance of different factors and assumptions in NWP-LES calculations for wind energy applications. Using a recent large ensemble of LES simulations driven by NWP boundary conditions over the complex terrain of the Perdigão area, our analysis reveals significant discrepancies in wind power estimates across ensemble members, particularly over hilltops. Depending on the model configuration and the coupling technique, instantaneous predictions can be as sensitive as 800kW for a 2MW wind turbine, in terms of ensemble standard deviation. On multi-day time averages, the model sensitivity is in the order of 150kW. We further analyze the main factors that lead to the observed model sensitivity. Results from a four-way ANOVA analysis identify topography and land use datasets as the primary drivers of variability, for time averaged estimates. Temporal analysis shows strong inter-daily variability and the importance of turbulence modeling and the coupling techniques for instantaneous predictions. Overall, most of the sensitivity is observed during day-to-night and synoptic transitions. By understanding the relative importance of different factors, future model development and applications can be guided to enhance the accuracy and reliability of wind energy assessments.

KEYWORDS
wind Power, Large Eddy Simulations, coupled meso-micro simulations, Perdigão, WRF-LES

1 | INTRODUCTION

The imperative need of transitioning current energy systems, heavily reliant on fossil fuels, to renewable and carbon-neutral energy sources is motivated by the need of addressing pressing environmental and societal challenges, including climate change, public health, energy security, and economic development. Many countries have set ambitious net-zero emissions targets, necessitating significant transformations, such as transitioning to renewable energy sources and increasing energy efficiency. Wind energy is a crucial component of these plans due to its cost-effectiveness and minimal environmental impact throughout its life-cycle. For example, the European Green Deal has established ambitious objectives for wind energy as a critical element of the region's shift toward a sustainable and carbon-neutral economy. Wind energy is expected to play a major part in achieving the goal of generating 60% of the region's electricity from renewable sources by 2030[1]. Individual countries have already made significant progress in achieving such targets. To date, Denmark remains the country with the highest share of wind power in its electricity mix, with wind power accounting for over 47% of Denmark's electricity generation[2]. The US has set a target of achieving 100% clean electricity by 2035, and wind energy is expected to play a significant role in achieving that goal. China is also a major player in the global wind energy market and has set ambitious targets for expanding its wind energy capacity. In its 14^{th} Five-Year Plan, China set a target of reaching 240 GW of wind power capacity by 2025, which will almost double the country's current installed wind capacity[3]. Decades of scientific advancements and technological progress have propelled wind

energy to become a mainstream source of electricity, accounting for nearly 7% of the world's total electricity generation[2]. Current studies suggest that wind energy alone could fulfill the world's entire energy demand by 2030[4,5]. Nevertheless, ongoing research and innovation are critical to meeting these expectations, as widespread use of wind energy will require technology to be pushed into uncharted territories, both scientifically and engineering-wise[6,7]. Additionally, continuous advancements are essential to ensure the cost-effectiveness and competitiveness of wind energy in the market[4,5]. Specifically, Veers[6] identified three primary challenges in wind energy research that must be tackled to enable an extensive and cost-effective utilization of wind energy: (i) a comprehensive understanding of the atmospheric flow dynamics within wind farms' operational zone, (ii) the aerodynamics and structural dynamics of larger wind turbines, both onshore and offshore, and (iii) a collaborative integration of wind farms into the future electricity grid. The present study contributes to the first objective by advancing understanding of atmospheric flow dynamics with numerical simulations for wind energy applications.

Quantifying and predicting wind speeds at turbine hub height requires understanding atmospheric dynamics and microscale flow properties within the planetary boundary layer (PBL), a task that is particularly challenging in regions of complex terrain[8], namely areas characterized by irregular topography and land use. Several studies have investigated microscale flows in complex terrain via high resolution numerical simulations, in idealized settings (e.g., with Large Eddy Simulations (LES)[9]) or via lower resolution Reynolds-Averaged Navier-Stokes (RANS) methods for Numerical Weather Prediction (NWP) applications, in realistic settings[10]. Accurate simulations of processes at such fine spatial scales also require acknowledgment that the microscale flow is influenced by larger mesoscale conditions, thus developing coupled meso- to micro-scale simulations is critical to obtain a realistic model output[11,12]. The meso- to micro-scale coupling is particularly challenging, as current meso- and micro-scale models rely on fundamentally different assumptions to resolve turbulence processes. Mesoscale models are based on the RANS approach, where the steady-state properties of the flow are of interest and key sub-grid scale physics processes (e.g., radiation transfers, surface and boundary layer processes, clouds, moisture) are parameterized. Conversely, microscale models, applied at finer resolution (i.e., tens of meters), either resolve turbulence from the Navier-Stokes equations through expensive direct numerical simulations (DNS) or through LES which parameterize small eddy scales. Major uncertainties and challenges still remain as how to couple meso- to micro-scale simulations and to properly simulate phenomena at gray zone (GZ) or Terra Incognita resolutions[13], which occur at around 1km and for which subgrid scale (SGS) parameterization assumptions on the grid size are violated with both RANS and LES[14]. As a result, unrealistic flow structures may be simulated if traditional closure techniques are not revised[15,16]. However, it is of high interest to perform simulations at such resolutions, as they are critical to: i) produce detailed numerical weather predictions (e.g., by improving representation of turbulent characteristics[17], resolving local flow characteristics related to topography[18] and land use[19]), ii) improve representation of the wind turbines impact on the atmospheric flow (e.g., wake effect[20,21]) and iii) provide appropriate boundary conditions to urban scale models (e.g., for urban heat island quantification[22]). While recent studies have explored new approaches to overcome these difficulties[23,24,25,26,27] and improve the accuracy and efficiency of multi-scale model runs (e.g.,[28,29,30,12]), a comprehensive understanding on the subject is still elusive[31,32].

Recent advances in high-performance computing now allow for high-resolution and multiscale simulations for wind energy purposes[33,34,17], where the coarsest LES domain is forced with boundary conditions generated by the finest mesoscale simulation. Large-scale tendencies are thus dynamically integrated in high-resolution simulations, thus overcoming several idealizations in canonical LES of the PBL[35]. This integrated approach is particularly important to study transient phenomena (e.g., frontal passages[36], thunderstorm outflows, baroclinic systems, low-level jets), changes in atmospheric stability associated with the diurnal-nocturnal cycle[37], topography-induced flow[38], as well as to link site-specific wind conditions to the long-term climatology of the area[37]. The latter plays a key role to provide reliable predictions of the annual energy potential of wind farms and reduce financial risks[39]. Short-term wind energy forecasts can also benefit from LES coupled with mesoscale simulations[40,41]. However, multiscale simulations are still in their early stage, are highly complex and require many input parameters and assumptions, potentially resulting in uncertainties in their outputs. In this study, we take advantage of a recent dataset of 36 multiscale simulations[42] to explore the sensitivity of wind energy estimates calculated with LES runs coupled with mesoscale forcing, with the goal of studying their uncertainty and sensitivity to different input factors. Specifically this work aims to:

1. Characterizing the time-resolved sensitivity and uncertainty of wind power production estimates with multiscale numerical simulations, for an isolated 78 m wind turbine in complex terrain (Perdigão field site);
2. Characterizing the spatial distribution of the sensitivity of multiscale simulations for wind energy purposes, to further elucidate the role of complex terrain;

3. Providing a benchmark study that can serve as a reference for wind energy assessments performed in areas of complex terrain with multiscale simulations.

This paper relies on simulations presented in Giani and Crippa[42] that focuses on PBL dynamics with the ultimate goal of investigating how different configurations of multiscale simulations impact wind energy predictions.

The remainder of the paper is organized as follows. In the next Section, we present the numerical simulation ensemble (Section 2.1), followed by the methodology for the sensitivity analysis (Section 2.2 and Section 2.3). The results from the sensitivity analysis are laid out in Section 3, where we address and discuss the temporal (Section 3.1) and the spatial (Section 3.2) distribution of variability within the ensemble. Thereafter, we investigate the sensitivity of power production in Section 3.3. Finally, in Section 4, we present the main findings, draw overall conclusions and outline potential areas for future research.

2 | MATERIALS AND METHODS

2.1 | Numerical meso- to micro-scale simulations

This work is based upon a recent ensemble of four-day long multiscale simulations[42] over the Perdigão field site (Portugal), which is characterized by two parallel double ridges and a small valley in between, in an area that is approximately 6x6 km^2 [43,44]. The two parallel ridges are about 1.5 km apart and are roughly 4 km long and 550 m high at their summit. The detailed description of the dataset can be found in Giani and Crippa[42], whereas here we report the main features of the simulations that are key to interpret the wind energy analysis presented in this work. Relevant experimental details[43] of the campaign and other modeling work over the Perdigão valley[44,45,46] can be found in recent literature.

In this work, we analyze an ensemble of 36 multiscale runs generated with the Weather Research and Forecasting (WRF) model version 4.4[47], that encompass five nested domains. The resolutions of the five different domains span from 11.25 km in the outermost domain to 30 m in the innermost one. The general circulation in the outermost domain is solved with a mesoscale turbulence parameterization (1D PBL scheme) while the flow in the innermost domain, that interacts with the double-ridge topography, is solved with microscale LES closures. The difference across the 36 configurations lies in four different input factors. Specifically, the ensemble runs include (i) different topography and land use datasets in the finest domains (*Topography*), (ii) different initial and lateral boundary conditions for the outermost domain (*LBCs*), (iii) different turbulence closures in the intermediate gray zone domains (*GZ treatment*) and (iv) different SGS models for the LES innermost domain (*SGS-LES*). Two different options are used for *Topography*, and include the default WRF coarse datasets (around 900m in resolution) and tailored fine datasets from NASA's Shuttle Radar Topography Mission (SRTM[48]) for topography and the Coordination of Information on the Environment (CORINE) for land use[49], that have 30 m and 100 m resolution, respectively. Three choices are used for *LBCs*, including the Global Data Assimilation System (GDAS) final analysis[50], the high-resolution operational data from the European Centre for Medium-Range Weather Forecast (HRES-ECMWF[51]) and ECMWF's ERA5 reanalysis[52]. Three choices are considered for *GZ treatment*, a traditional 1D PBL scheme (The Yonsei University Scheme, YSU[53]), the scale-aware version of YSU (Shin-Hong[26]) and Zhang's 3D blending closure[23]. Finally, two options are tested for *LES-SGS*, the Turbulent Kinetic Energy (TKE) closure of Deardorff[54] and the deformation-based Lilly-Smagorinsky closure[55,56]. Each combination of the different options of the four different input factors is available in the dataset, i.e. in total there are $2 \times 3 \times 3 \times 2 = 36$ simulations. More details about specific choices of the input factors can be found in Giani and Crippa[42].

The simulations cover four days during the Intensive Operation Period (IOP) of the Perdigão field experiment, from May 19, 00 UTC to May 23, 00 UTC. Note that the local time is UTC+1 during the simulated episode. During the simulation days, no precipitation and a mixture of clear sky days and high and medium clouds are observed. The episode is characterized by a periodic passage of low and high pressure, and towards the end of the simulation time synoptic and local winds decrease substantially.

2.2 | Four-way Analysis of Variance

The goal of this work is to disentangle the effect and the relative importance of the four different input factors described in the previous section on time-resolved wind energy calculations at a specific point in space, where a 78 m tall wind turbine is, as well as across the simulated spatial domain. We focus on the innermost domain, discretized at 30 m resolution, which is solved

with the LES technique in the 36 configurations described in the previous section. To evaluate the sensitivity of the dataset to various input factors, we conduct a four-way Analysis of Variance (ANOVA[57]). By decomposing the variance, this analysis identifies which factors have the greatest impact on variability across the ensemble members. As a result, this investigation may help with future simulations optimal design by providing insights on ways to reduce uncertainties. It will also help save computational resources by identifying factors/setup the model is most sensitive to, thus improving the overall robustness of the multiscale simulations.

To assess both the spatial and temporal variability of the model output, we conduct two separate analyses. The spatial analysis covers the entire innermost domain, while the temporal analysis focuses only on the turbine site. Both analyses examine the relationship between wind speed at 78 m and power production. Further, we conduct the sensitivity analysis for both the entire simulated time period and four specific sub-periods of interest: (i) *daytime* (12-15 UTC), which featured a fully developed convective boundary layer (CBL); (ii) *late afternoon* (16-20 UTC), which represent the transition period from daytime to nighttime; (iii) *nighttime* (00-03 UTC), when stable boundary layer conditions prevail; and (iv) a period characterized by a change in synoptic conditions (May 21, 12 UTC to May 22, 06 UTC), when both the prevailing wind direction and wind speed vary significantly (*synoptic transition*). Here we introduce the fundamental concepts of a one-way ANOVA, and then generalize it to a four-way version.

Let x_{ij} be run j in group i, so for example x_{13} is the third element in first group. If we consider the *LBC* factor for the one-way anova, the three groups are the three options for *LBC*, i.e. GDAS, ERA5, HRES-ECMWF. From simple algebra, each individual element of the dataset can be decomposed as:

$$x_{ij} = \overline{x} + (\overline{x_i} - \overline{x}) + (x_{ij} - \overline{x_i}), \quad \forall i = 1, ..., K, j = 1, ..., N \tag{1}$$

where $\overline{x}$ is the grand mean (average of all 36 experiments) and $\overline{x_i}$ is the mean of group i. In our notation, K refers to the total number of elements per group and N refers to the number of groups (for instance, in the case of *LBC*, $N = 3$ since we have three options for the lateral and initial boundary conditions, and $K = 12$, where we are assuming that each group has the same amount of elements, which is true in our case). Thus, each individual wind prediction is equal to the sum of the grand mean, the deviation of the group mean from the grand mean, and the deviation of the individual prediction from the group mean. According to the decomposition of Equation 1, measures of dispersion within the ensemble can be computed as follows:

$$s^2_{explained} = \frac{1}{KN} \sum_i \sum_j (\overline{x_i} - \overline{x})^2 = \frac{1}{N} \sum_i (\overline{x_i} - \overline{x})^2 \tag{2}$$

$$s^2_{residual} = \frac{1}{KN} \sum_i \sum_j (x_{ij} - \overline{x_i})^2 \tag{3}$$

The explained variance indicates the extent to which group means match the grand mean, thus large values of $s^2_{explained}$ indicate large departures among the means of the three groups. The individual terms $(\overline{x_i}-\overline{x})^2$ quantify how much of the ensemble variability is explained by differences in each factor. The residual variance, instead, quantifies differences within each group and consequently computes the amount of variability introduced by other factors. Given the law of total variance, the sum of the previous two quantities equals total ensemble variance:

$$s^2_{total} = \frac{1}{KN} \sum_i \sum_j (x_{ij} - \overline{x})^2 \equiv s^2_{explained} + s^2_{residual} \tag{4}$$

A four-way ANOVA is a variation of a one-way ANOVA and calculates the corresponding $s^2_{explained}$ for each individual input option and allocates the remaining variance to $s^2_{residual}$. Additionally, when multiple factors are analyzed, interaction effects may contribute to the variance. For a four-way ANOVA, six interaction terms among two factors, three interaction terms among three factors and one interaction term among all factors can be considered. However, if interactions are excluded, as in this work, the residual variance will account for their contribution. In other words, the residual variance can be decomposed into the sum of all the 10 interaction factors. We use the software *R* to compute the four-way ANOVA. It is worth noting that our case is a balanced dataset case, and therefore the order that different terms are inputted into `anova()` function is unimportant. Each

group consistently has an equal number of elements. Therefore, the decomposition of total variance for a multi-way ANOVA can be expressed as follows:

$$\sum_{m=1}^{M} s^2_{explained,m} + s^2_{residual} = s^2_{total} \tag{5}$$

where M is the number of factors (i.e. M=4 in our case).

2.3 | Power curve and wind energy production

We focus on the time-resolved sensitivity analysis of the 36 multiscale simulations at one specific point in the domain, before expanding the discussion to the entire spatial domain. The specific point that we consider is co-located with an ENERCON E-82 E1 wind turbine, with a height of 78 m and a rated power of 2 MW. The wind turbine is located on the south-west ridge (39.708N, 7.745W) and has been in operation since 2007. The model sensitivity over the whole time series of both wind speed and power production is tested at the numerical grid point closest to the wind turbine location. The following power curve is used to estimate wind power production based on the simulated wind speeds at turbine hub height. As shown in Figure 1, the cut-in wind speed for power to be generated is about 2 m s^{-1}. After that threshold is met, wind power increases approximately with the third power of wind speed until it reaches the rated speed at 13 m s^{-1}. Further increases in wind speed will not affect power production, which remains constant at the wind turbine rated power (2 MW). However, if the wind speed exceeds the cut-off value (25 m s^{-1}), the turbine is not allowed to deliver power to prevent excessive stress on the structure. The impact of the 36 model configurations on wind power is also analyzed through ANOVA, as small discrepancies in wind speeds among runs may lead to significant differences in power and energy production levels, given the non-linear relationship between wind speed and wind power.

3 | RESULTS

3.1 | Temporal variability of wind speed at the turbine site

In this section, we present simulated wind speed data extracted from the 36 ensemble members at the turbine location at hub height (Figure 2). Although a full model evaluation is beyond the scope of this study, we briefly compare the simulated wind speeds with the observed values at the closest meteorological mast that include near hub-height measurements (100m). The meteorological mast was located on the South-West ridge (39.706N, 7.744W) and its code for the Perdigão field campaign is *tse04*. The observations reveal a clear diurnal cycle, with wind speeds decreasing during convective daytime conditions and increasing at night, a trend that is generally captured by all model runs. However, during the synoptic transition on late May 21 and May 22, a notable shift in the typical diurnal cycle is observed. Specifically, the wind direction shifts from ENE to SSW, the wind speed drops, and the typical nighttime increase in wind speed is not observed. This perturbation is driven by weaker winds aloft, as well as by a change in wind direction that precludes the typical wind speed amplification observed on the second/downwind ridge, where the turbine is located, when there is a northeasterly flow.

The analysis of the four periods of interest reveals that the ensemble average over the entire time period closely matches the observed data, as shown in the whole timeseries boxplot in Figure 3. However, a closer examination of the data indicates that the model tends to overestimate wind speeds by approximately 1.5 m s^{-1} during the daytime and late afternoon periods and underestimate it by roughly the same amount during nighttime. The different model setups adopted do not have a significant impact on the discrepancies across the ensemble members, as highlighted by the small spread between the 1^{st} and 3^{rd} quartiles of approximately 0.5 m s^{-1} during daytime and late afternoon periods. During these time periods, the model consistently exhibits a positive bias against the observed data. The variability across the ensemble members also varies through time, with the largest variability occurring during nighttime and synoptic transition periods. For example, on May 22, during the synoptic transition characterized by a shift to a southerly flow, the wind speed is weaker on average compared to the previous nights and similar to the day-night transition. However, the spread across the ensemble runs is larger during this period (Figure 3), indicating higher uncertainty in the model's ability to accurately capture the wind speed variability. This highlights the importance of different

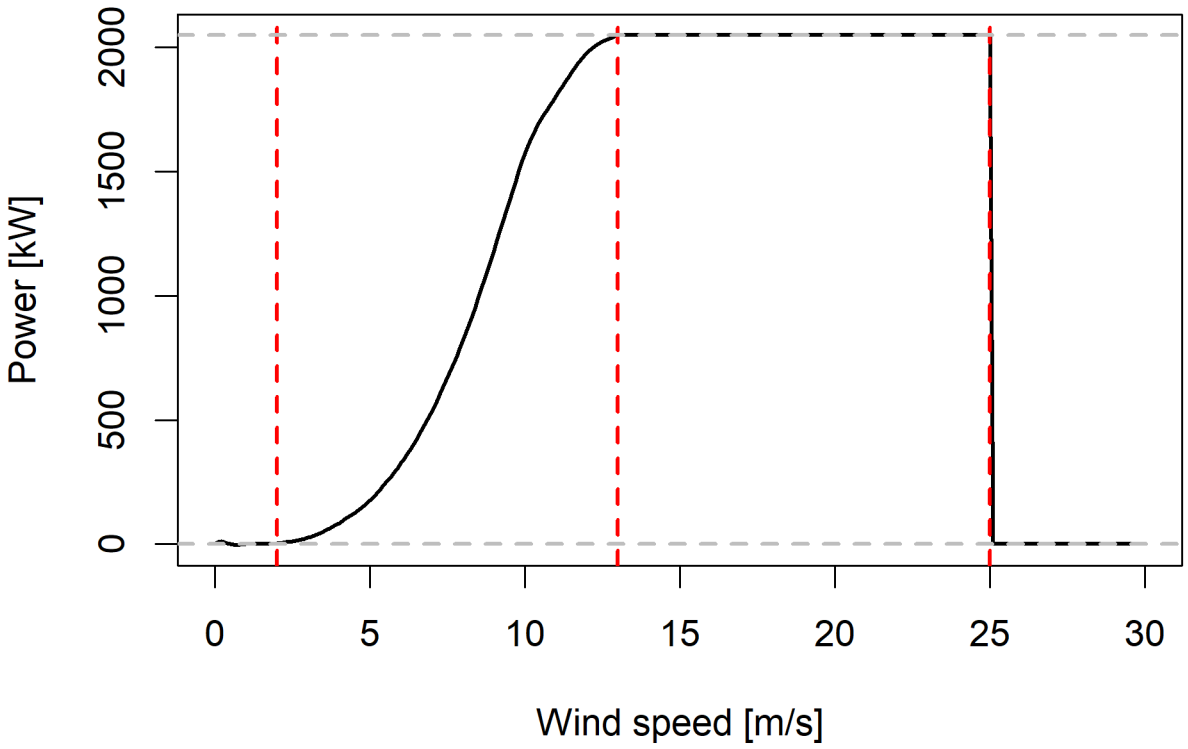

FIGURE 1 ENERCON-2MW wind turbine power curve[58]. Dashed red lines represent the cut-in speed, rated speed and cut-off values, from left to right.

parameterizations or forcing in generating uncertainty across runs. These results demonstrate that the model does not capture all the PBL dynamics equally well and struggles the most during nighttime and stratified flow conditions.

As this preliminary analysis indicates that there are significant differences in the wind speed estimates among the ensemble members over time, we conduct a sensitivity analysis to identify the sources of discrepancy and spread across the ensemble members with respect to each of the four factors under examination. This investigation is aimed at contributing to a better understanding of model's limitations and strengths and provide insights into ways to improve its performance. Specifically, a sensitivity analysis is performed over wind speeds averaged either over the whole timeseries or over the individual four sub-periods of interest at the turbines hub height. Figure 4 illustrates the total variance (in gray) and how it is broken down across factors. With the exception of the synoptic transition, it is observed that topography is the primary factor contributing to 40-80% of wind speed variability across runs. This can be attributed to the spatial resolution of the various topography products used. The coarser terrain dataset, which is the default in WRF, considerably smooths the terrain and have a large impact on the wind predictions. Furthermore, having a smooth three-dimensional hill rather than a double ridge topography may have led to inaccuracies in the simulation of mountain-valley flow and thus generated discrepancies across the runs. The surface roughness is also quite different between the coarse and fine land use datasets, and it is expected to generate differences in near-surface quantities[42], because of the presence of non-negligible canopy[59]. During daytime and nighttime periods, the LBCs and the GZ treatment also contribute to the spread, each by more than 20%, whereas their impact is much less relevant during other time periods (i.e., day-night transition and whole-day averages). As far as the synoptic transition is concerned, the LBCs factor mostly drives discrepancies in wind speed estimates at the microscale, by contributing to 45% of total variance. Here, topography only accounts for 24% of the variability across runs. This is most likely due to the mesoscale nature of the phenomena that govern the PBL under changes of synoptic conditions as the one occurring on late May 21 and May 22. Therefore, when simulating synoptic transition circumstances great emphasis should be placed on how initial and later boundary conditions for the outermost domain are defined. The SGS model adopted is generally the least relevant factor, contributing to about 1% of the total variability across runs. This is a somewhat surprising result, as previous idealized studies suggested that

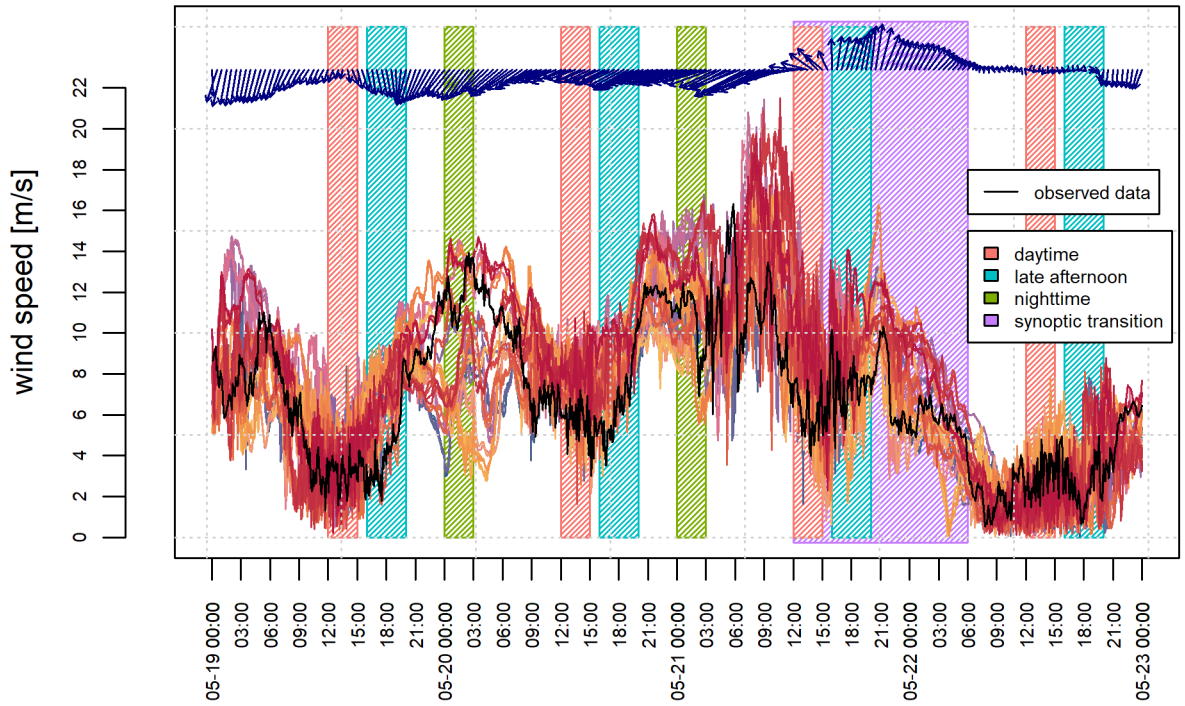

FIGURE 2 Temporal variability of simulated wind speed (m s^{-1}) at the turbine location at hub height (i.e., 78 m) across the 36 ensemble members. Observations are in black and the arrows on top represent the hourly mean direction the wind is blowing to and the length of the bar is proportional to the mean wind speed across the ensemble runs. The vertical bars indicate the hours used in the analyses over specific period of interest defined in Section 2.2 (i.e., *daytime*, *late afternoon*, *nighttime* and *synoptic transition*).

SGS modeling is important for the velocity spectrum as well as the velocity field[60,61], but in the context of our real case dataset it appears to have a marginal role compared to other modeling choices (e.g., *LBC*).

Finally, the decomposition of variance performed on the individual five-minutes data over the whole time series is presented in Figure 5 and indicates some inter-daily variability. Occasionally, a single factor may persistently prevail over the others for a certain time frame (e.g., gray zone treatment on the first night). However, a consistent daily pattern cannot be inferred. On May 19 and May 20, the largest total variance is found at night, consistently with the results presented in Figure 3. However, this is not the case on May 22 and May 23, where constantly high and low variances are observed throughout the two days, respectively. On May 23, none of the four factors is found to dominate during the last day, which can be interpreted in light of the overall small variance associated with the low simulated wind speeds. As discussed earlier, the change in synoptic conditions might be responsible for this pattern, which is also reflected in the large variance explained by *LBC* between 12 and 18 UTC on May 21. The five minutes analysis allows further identifying interesting phenomena that are not revealed by the time-averaged analysis. For example, during the night between May 19 and May 20, the vast majority of the spread within the ensemble can be traced back to how turbulence has been modeled at gray zone resolutions. Conversely, as previously shown in Figure 4, nighttime averaged variances show that topography is the leading factor in explaining the model sensitivity. Note that the average of the variances in Figure 5 is different from the variance on the wind averages, as compensating effects between large and low values of wind speed in different simulations can effectively lead to negligible variance on the winds time averages. In conclusion, it can be stated that when a time aggregated analysis is of relevance, as in the cases of optimal turbine siting and regional climatology, topography and land use datasets are the leading factors in determining the *time-averaged* wind speeds. The reason is that lower or higher surface roughness, for instance, consistently lead to higher and lower wind speed, respectively, biasing the time averages. On the contrary, when a prediction with a short time resolution is of interest as in the case of hourly forecasts necessary to match the energy demand, different results should be expected. Dynamical analyses[42] are needed to investigate the physical mechanism underlying specific sensitivity patterns and thus help generalize current results.

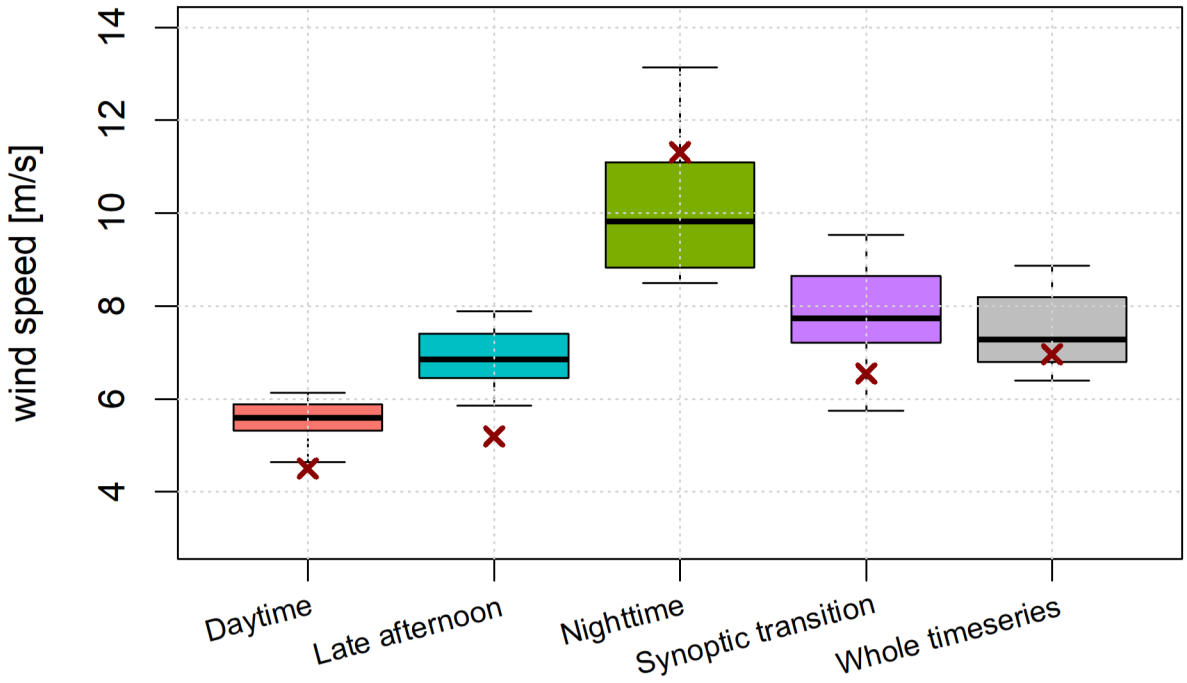

FIGURE 3 Time-averaged wind speed at the turbine height and location for each sub-period of interest and for the whole simulated period. Each whisker extends to the furthest data point that is within 1.5 times the interquartile range (IQR). The red cross shows observations at *tse04* averaged during the same time periods.

3.2 | Spatial sensitivity of wind speed to model setup

In this section, results of the sensitivity analysis performed over the the entire innermost domain are presented. The goal is to characterize the spatial distribution of the sensitivity of multiscale calculations of wind speed and thus investigate the role and the consistency in space of each of the four factors under examination. To this end, a four-way ANOVA has been carried out in each grid point on time-averaged wind speeds at the turbines hub height (78 m). Figure 6 shows the variance explained by each factor variable, displayed on a logarithmic scale. Each row represents the five sub-periods of interest over which time-averaged wind speed has been computed. Regardless of the sub-period, results show a significant influence of topography and land use datasets choices on the wind speed estimates, especially on the two parallel ridges and on the deepest section of the in-between valley (upper-left area), where the total variance itself is higher compered to the rest of the domain. As also highlighted in Section 3.1, a different accuracy in characterizing the topography of the area may have led to significant differences in the simulation of the mountain-valley flows and thus generated discrepancies within the ensemble. On the contrary, in all sub-periods and over the whole spatial domain, the model is insensitive to the LES SGS model, as also found with the time-resolved analysis. During nighttime and the synoptic transition, other factors gain importance, as shown in Figure 7. In particular, these effects are visible on the second ridge downwind (the SW and NE ones, respectively for *Nighttime* and *Synoptic transition*) where discrepancies among simulation members are higher, as well as in the flat region further downwind (respectively, lower-left and upper-right corners). Furthermore, it is of interest to note that in the deepest region of the valley it is again only topography that leads to substantial differences in wind speed estimates within the ensemble. Under both synoptic transition and nighttime conditions, whens variance is higher, a portion of total variance is explained by the residuals. As interactions of all orders between additive terms are not allowed in the current ANOVA model, residuals account for them all and thus for the variability introduced by varying two or more factors simultaneously. ANOVAs with first-order interactions have shown prevalence of interactions of topography, LBCs, and GZ treatment as most relevant ones (not shown). Therefore, when nocturnal time-averaged wind fields are of interest, the focus should be reserved to how all factors but LES's SGS model are modeled. Lastly, an area of numerical instabilities is observed at the northwest edge of the northern ridge, which is most likely a result of the limited capability of WRF hybrid hydrostatic pressure terrain-following coordinates to accurately simulate very steep

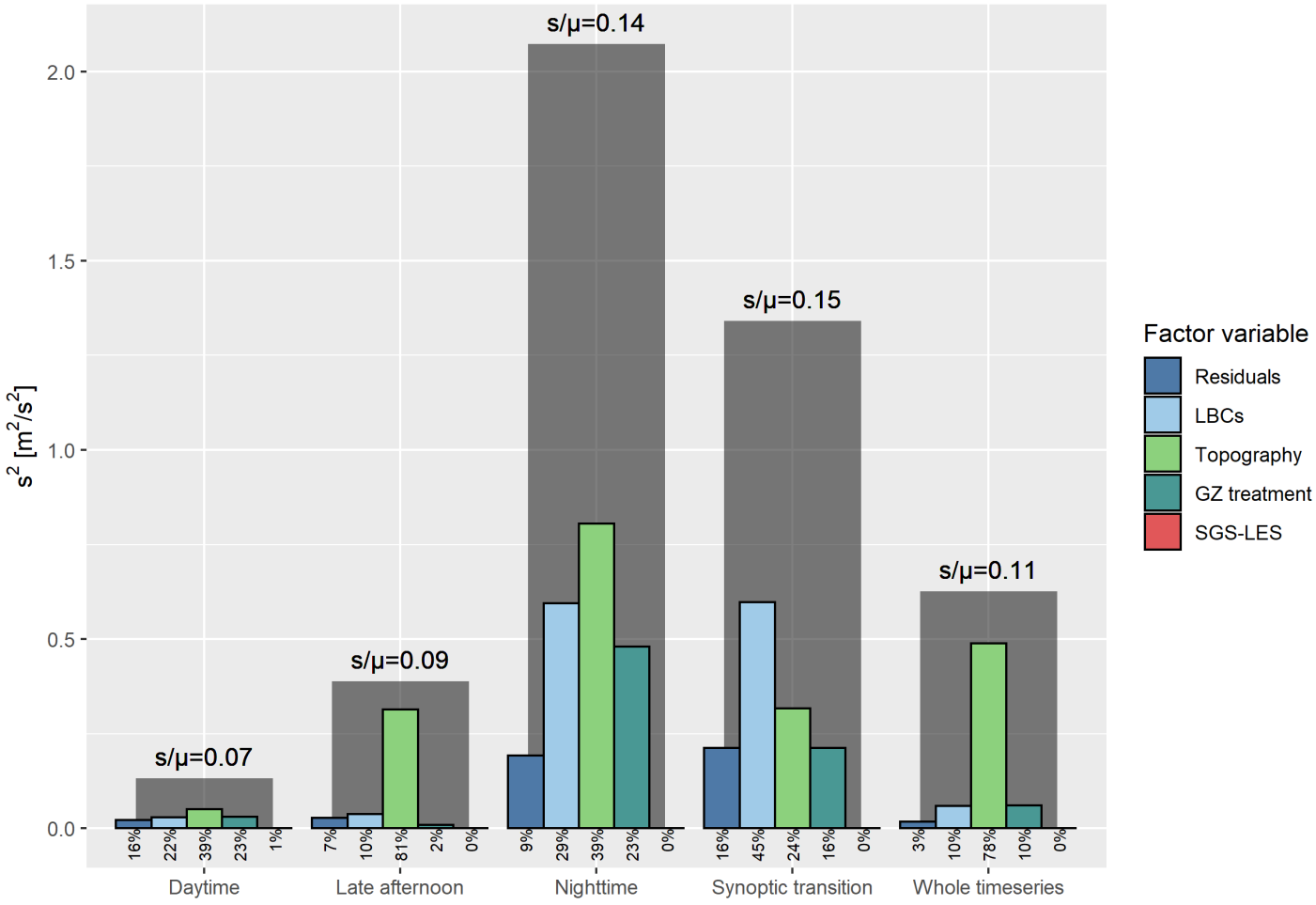

FIGURE 4 Decomposition of total variance (in gray) of time-averaged wind speed, among factor variables. Wind speeds have been simulated at the turbine site and at 78 m. On top of the gray bars, is the coefficient of variation (i.e., standard deviation divided by the mean) is shown, while at the bottom of each colored bar, the percentage of explained and residual variance is displayed.

slopes close to numerical boundaries (not shown). This is reflected in the non-negligible portion of variance explained by the LES SGS model in that area, suggesting that different subgrid scale models play a role in dissipating the numerical instabilities created by the fast horizontal and vertical velocities in the steep region of the domain (slope angles greater than 45 degrees).

In summary, when simulating multi-day averaged wind speed in complex terrain through multiscale simulations, as well as for daytime and late afternoon sub-periods, the elevation mapping and the land use dataset chosen for the site mostly drive the spread within the ensemble. This holds particularly true over ridges and in the valleys in between. With the exception of LBCs in the daytime, the other factors under examination do not significantly influence wind field simulations. When nighttime and synoptic transition wind speeds are of interest, instead, also the resolution and temporal forcing of global dataset, as well as the representation of turbulence in the gray zone are of relevance in dictating discrepancies in wind speed estimates. In Table 1, an overview of these findings is presented. In each entry, mean values of the variance explained by each factor computed over the whole innermost domain are given. Results are presented as percentages of the mean value of total variance, which is instead displayed in the last column in $m^2\ s^{-2}$.

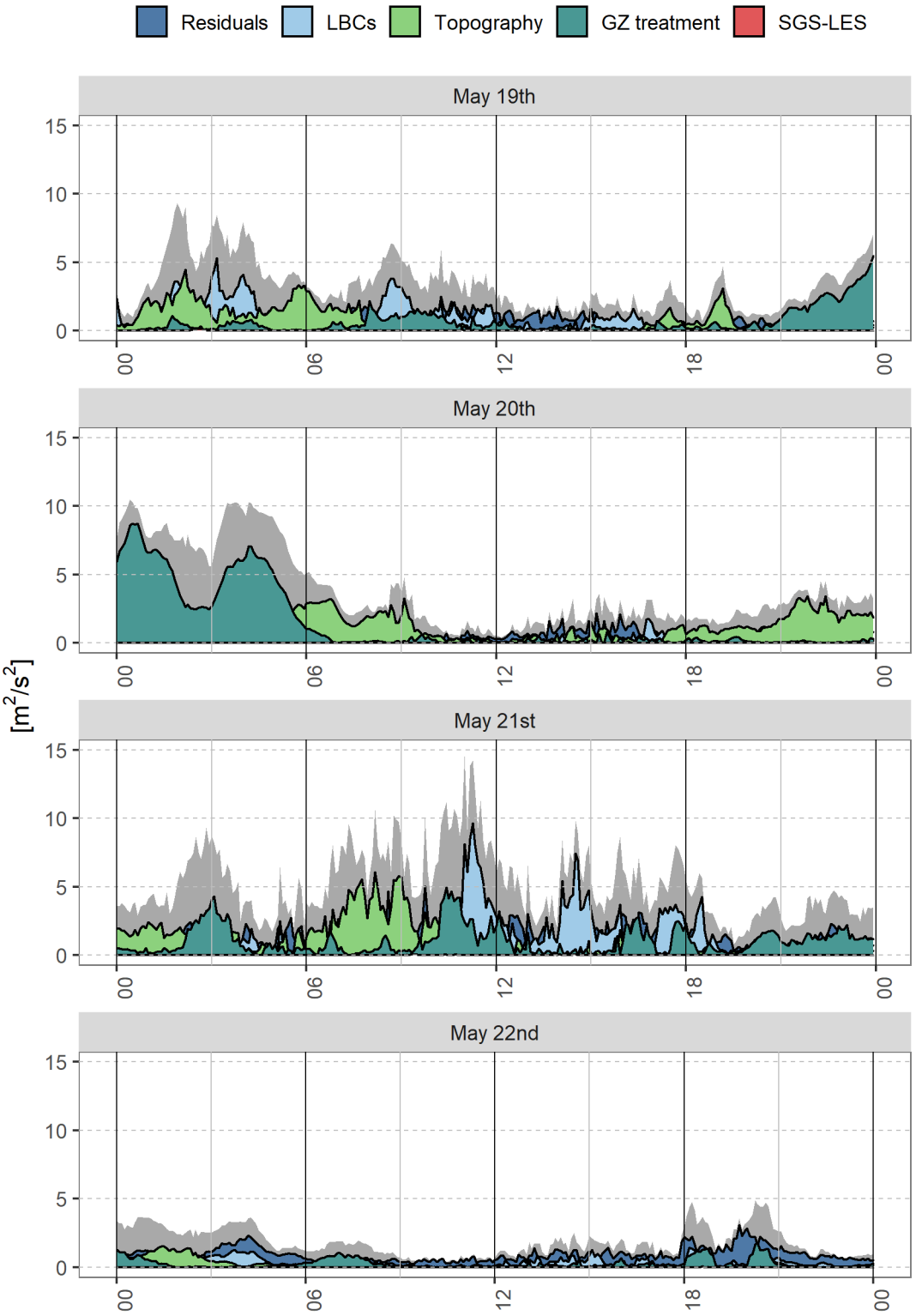

FIGURE 5 Decomposition of total variance [m^2 s^{-2}] of wind speed at 78 m above ground at the turbine site on each simulated day. The total variance is reported in gray.

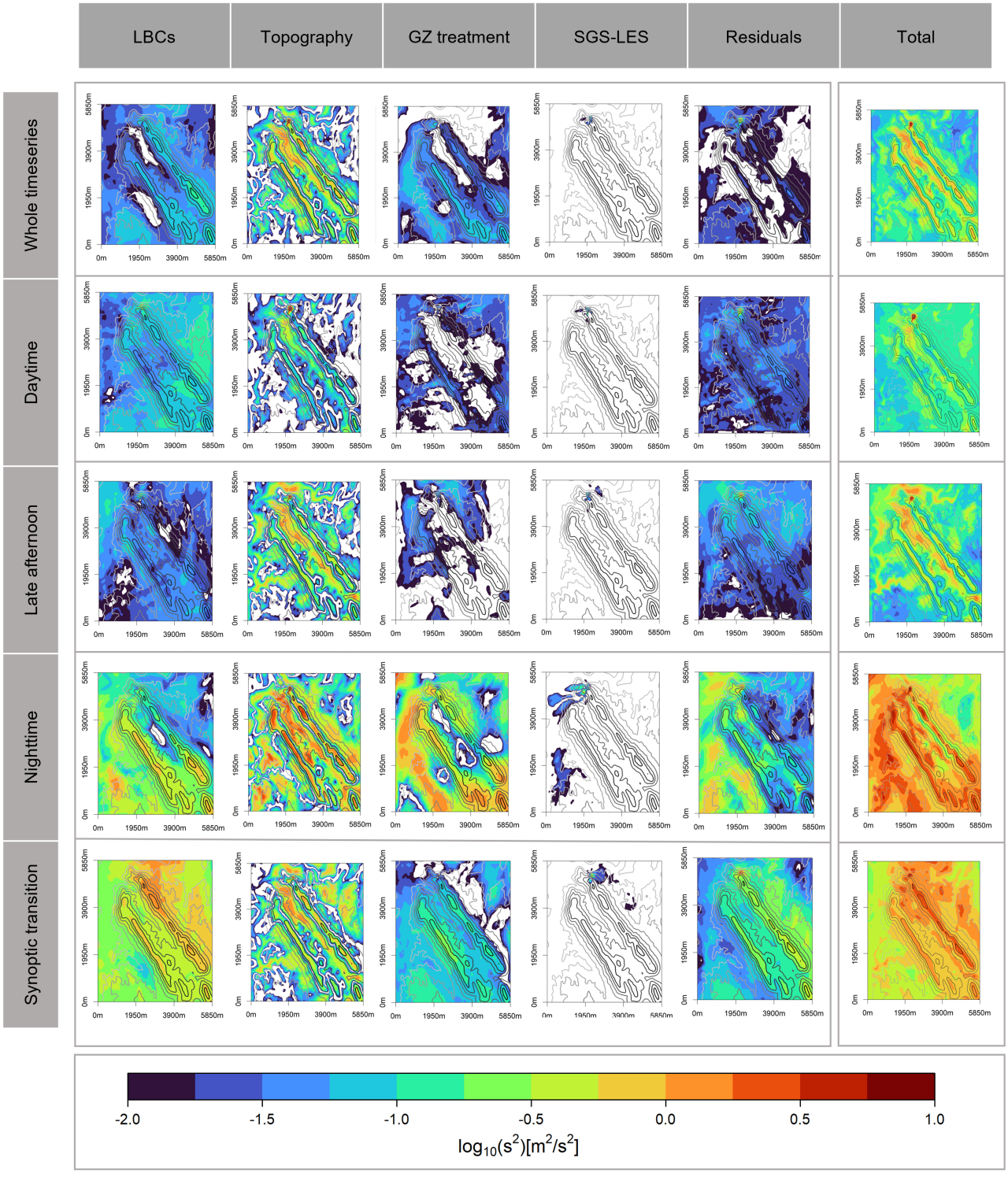

FIGURE 6 Variance explained ($m^2\ s^{-2}$) by each factor over the whole time series and the individual four periods of interest. The last column shows the part of variance not explained by the adopted ANOVA model. Note the $\log_{10}$ scale of the colorbar. In white, variances of less than 0.01 $m^2\ s^{-2}$ are shown. X and Y axis are displayed as distances in meters from the most South-West point of the domain (39.685N, 7.774W). The topography contours are showed in gray colorscale.

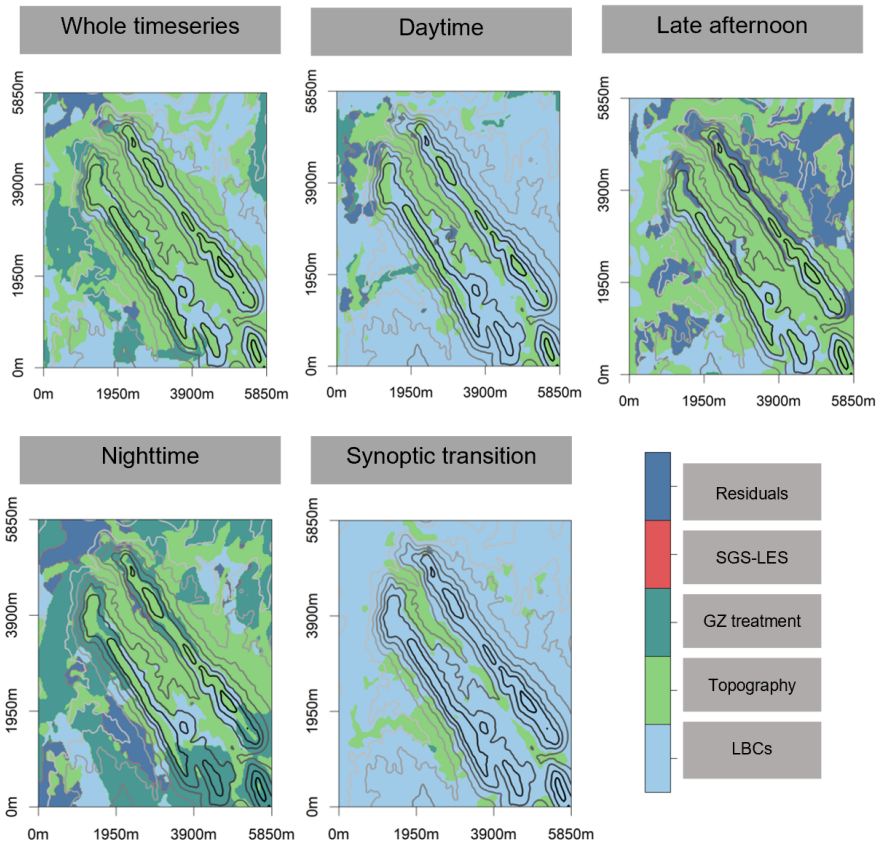

FIGURE 7 Factors explaining most of the variance at each location and time period. X and Y axis are displayed as distances in meters from the most South-West point of the domain (39.685N, 7.774W).

TABLE 1 Mean values of the variance explained by each factor when simulating wind speed in different time frames (columns 1-5, in percentage) computed over the whole innermost domain. Residuals account for interactions of all orders. Results are shown as percentages of the spatial mean of total variance (m^2 s^{-2}), which is presented in the last column.

	LBCs	Topography	GZ	SGS-LES	Residuals	Total (m^2 s^{-2})
Whole Period	19.5	60.9	12.7	0.29	6.69	0.219
Daytime	42.9	29.5	10.8	0.46	16.4	0.160
Late afternoon	14.5	62.9	5.54	0.30	16.7	0.234
Nighttime	19.4	32.9	32.3	0.32	15.0	1.142
Synoptic transition	55.4	21.6	7.81	0.21	15.0	0.848

3.3 | Sensitivity of wind power production at the turbine site

In this section, we examine how various modeling approaches affect the power generation predictions. Our focus is on the particular location where the wind turbine is situated on the southern ridge of the Perdigão domain. Although we can apply our findings to any point within the study area, we concentrate on this specific reference site as a realistic application with an existing wind turbine. In addition, measurements st *tse04* enable the comparison of power production estimates obtained from the WRF-LES simulated wind speeds with those from the actual observations. Figure 8 illustrates the fluctuation of wind power generation over time among the ensemble members and in comparison with the measurements. Similarly to the wind speed in Figure 2, the power production peaks over nighttime and is lowest during daytime periods, with a mean of 1390

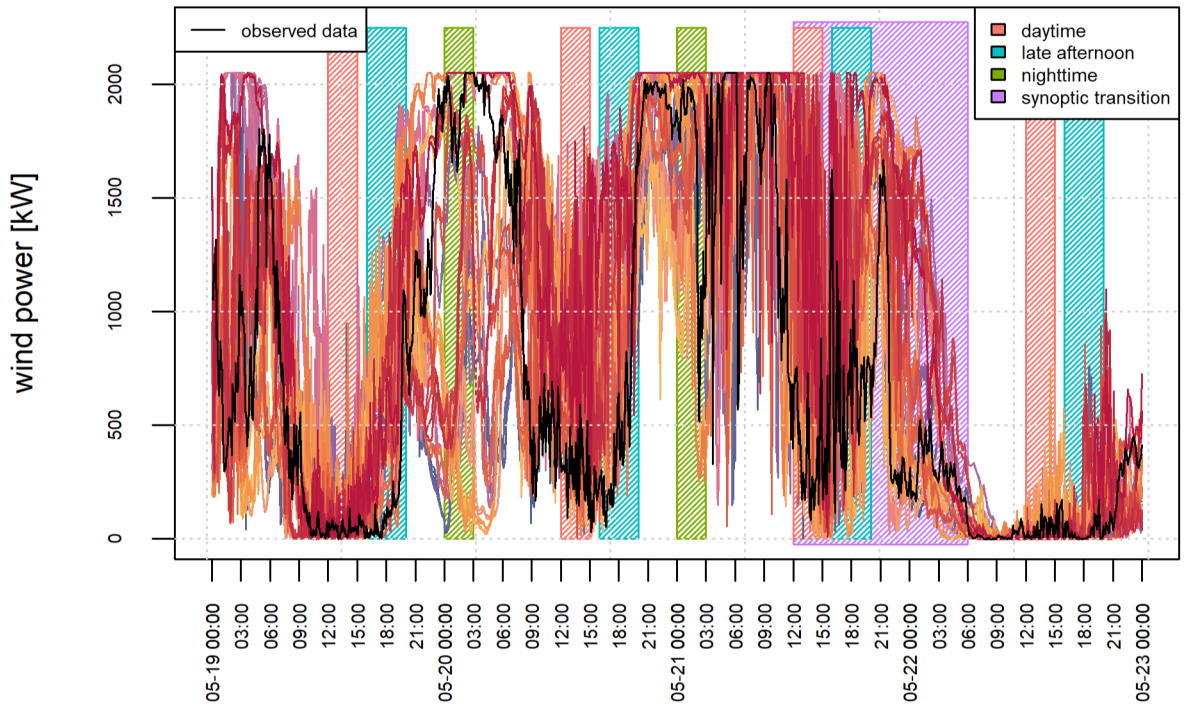

FIGURE 8 Power production estimates [kW] for an ENERCON-2MW turbine derived from the simulated wind speeds at 78 m at the location of the existing wind turbine on the southern ridge. The different lines represent the wind power generated using wind speeds from different ensemble members. The black line refers to the power estimated from the observed wind from a nearby meteorological mast (*tse04*), at near hub height (100m).

kW and 490 kW, respectively. While the mean wind speed over the entire time period analyzed only slightly overestimates observations (see Figure 2), the model bias for the mean power production is much larger, 840 kW from the model versus 525 kW from observations. Namely, a 37% average power difference is found for the ensemble mean, while the same wind speed bias in percentage was only 7%. The imbalance increases in all sub-periods, although it is during daytime that the highest difference is found, as the discrepancy between observations and ensemble mean is equal to 74% of latter (19% for wind speed). This can be explained by considering that the power production generally scales with the cube of the wind speed (see Figure 1), thus biases in wind speeds may be significantly amplified when estimating wind power. As expected, the variability among the ensemble members is also amplified in relation to the wind speeds, as demonstrated in Figure 9. The coefficient of variation (CV), displayed on top of each bar in both Figure 4 and Figure 10, is used to quantify and compare such differences. Values of CV (the standard deviation between ensemble members divided by the ensemble mean) are twice or even three times (during daytime) higher compared to their wind speed equivalents. In the case of wind power, the greatest variability within the ensemble is found during the period of synoptic transition (coefficient of variation equals to 0.31), although the greatest variation in absolute terms occurs in nighttime as its standard deviation is 305 kW, against the 270 kW of synoptic transition. For comparison, the average electricity power consumption for a single American household is approximately 1.2 kW, from U.S. Energy Information Administration[62] estimates. Therefore, the ensemble power variability across the ensemble is significant, highlighting the importance of further constraining multiscale LES calculations to have a highly accurate and reliable simulation tool for realistic applications. During the daytime and late afternoon time periods, as well as for averages over the whole four-day period, discrepancies between ensemble members are halved if compared to other periods. However, they are still significant and not negligible. It is also worth noting that during the first and last daytime periods, some simulations indicate very low wind speeds (below 2 m s^{-1}), resulting in zero power generation, as per the power curve. Similarly, wind speeds exceeding 13 m s^{-1} that are simulated during most nighttime periods fall within the rated power of 2000 kW for the installed turbine. Consequently, the bias between the observed and simulated power levels off during these periods.

Here we present results from the ANOVA decomposition of variance performed over different time averages of power production estimated from the simulated winds at the turbine site. Figure 10 displays similar patterns to the ones of wind speeds

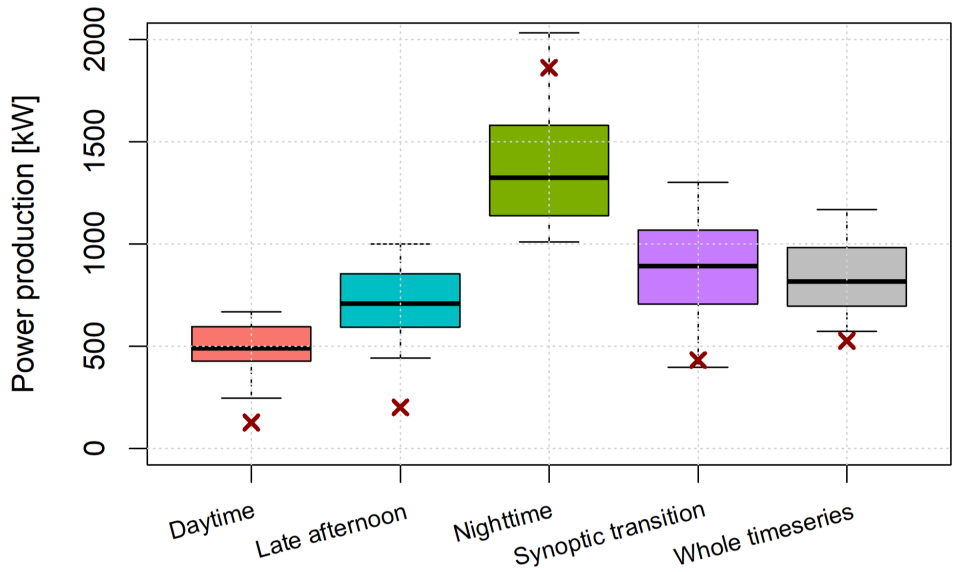

FIGURE 9 Time-averaged wind power at the turbine height and location for each sub-period of interest and for the whole simulated period. Each whisker extends to the furthest data point that is within 1.5 times the IQR. The red cross shows wind power computed from the observed wind speeds.

(Section 3.1, Figure 4). When the whole time series and late afternoon are analyzed, topography resolution still appears to be a dominant factor in explaining the variability in power production across runs, with a contribution of around 70%. During synoptic transition, as it was in the previous analysis, the model is most sensitive to LBCs, whose different characterizations account for 44 % of total variance. Yet, in other sub-periods some discrepancies in sensitivity patterns compered to wind speed analyses can be noted. Given the characteristic power production curve (detailed in Section 2.3), whenever the input wind speeds are either below 2 m s^{-1} or exceed 13 m s^{-1}, the power production saturates, as depicted in Figure 8. Therefore, when all simulations exhibit wind speeds either below 2 m s^{-1} or above 13 m s^{-1}, an increase in wind speed does not result in an increase in power generation, and the spread among the simulated wind speeds leads to equal power production estimates, pushing variance to zero, and making it insensitive to all factors. Similarly, when only certain runs of the ensemble simulate wind speeds above or below these thresholds, the relative importance of each factor may vary as well compered to previous sensitivity analysis on wind speeds. This is the case of nighttime and daytime sub-periods. As captured in Figure 2, indeed, during the first two nights certain runs simulate winds that blow faster than 13 m s^{-1}, while during May 19 and daytime hours of May 22 wind speed occasionally drops below 2 m s^{-1}. Consequently, main explaining factors of total variance differ from previous wind speed ones. In particular, in both nocturnal and diurnal hours, the effect of topography is reduced, in favor of LBCs (52 %) and GZ treatment (45 %), respectively for daytime and nighttime. In conclusion, it should be taken in consideration that, under specific wind conditions (wind speeds of about 2 or 13 m s^{-1}), improvements of those input features highlighted by wind speed sensitivity analyses may not necessarily enhance power production estimates, and vice versa.

Same conclusions can be drawn for sensitivity analysis performed on five-minutes power production simulations, whose decomposition of variance is presented in Figure 11. Generally, similar sensitivity patterns of wind speed analysis can be seen. However, 'deformations' due to the characteristic power curve of wind turbine are still visible. An illustrative case is set by May 21. On the one hand, during the early hours when wind speed are consistently above 13 m s^{-1} in some simulations, decomposition of variance of wind power returns an altered sensitivity pattern if compared to previous results on wind speed, characterized by the absence of predominance of any factor. On the other hand, after 12 UTC, when wind speed starts dropping and the simulated wind direction begins to shift from ENE to SSW starting synoptic transition, the same pattern of the wind speed analysis can be detected, characterized by the dominance of LBCs effects, overtaken by the gray zone treatment as the sun sets. The only difference is the magnitude of the curves, here amplified by the characteristic cubic shape of power curve when wind speeds are well between the range 2-13 m s^{-1}.

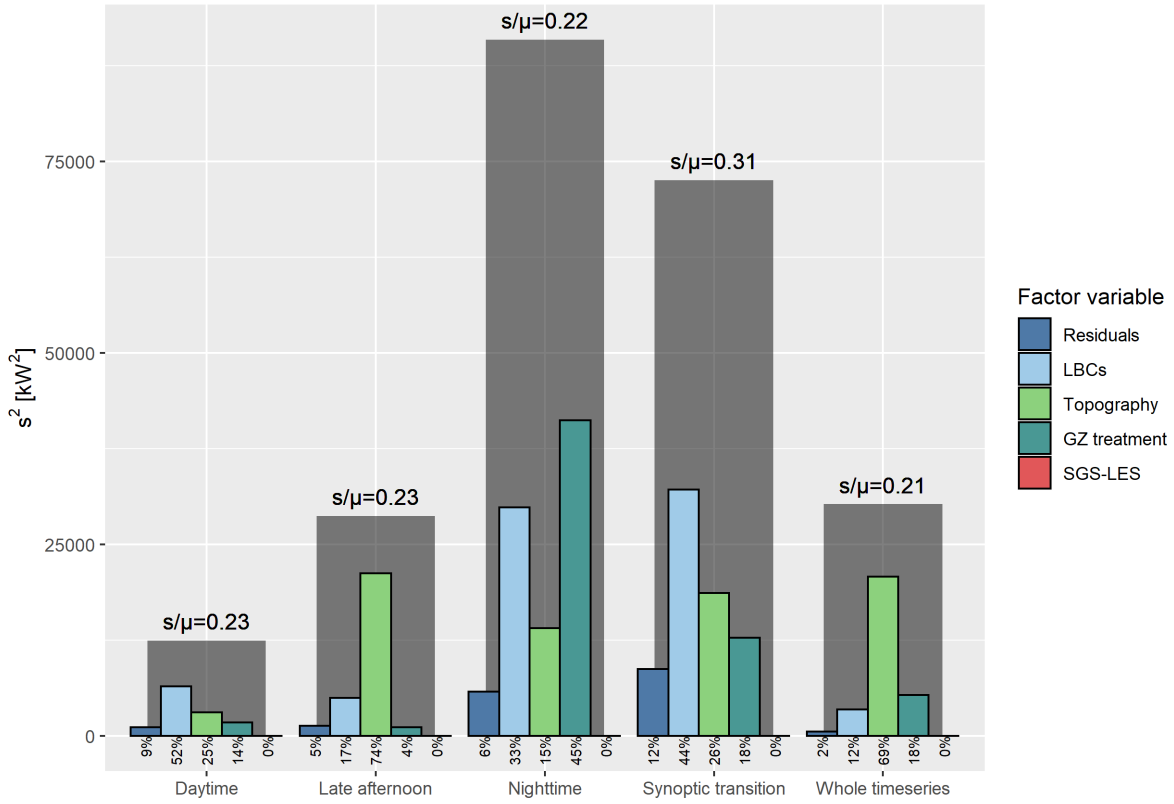

FIGURE 10 Decomposition of total variance (in gray) of time-averaged power productions, among factor variables. Wind speeds have been simulated at the turbine site and at 78 m above ground. On top of the gray bars, the coefficient of variation (i.e., standard deviation divided by the mean) is shown, while at the bottom of each colored bar, the percentage of explained and residual variance is displayed.

4 | DISCUSSION AND CONCLUSIONS

Multiscale modeling tools have the capability to simulate atmospheric motions across a broad range of spatio-temporal scales, covering almost all turbulence energetic scales. By using a coupling technique that bridges meso- and micro-scales, high-resolution nested Large-Eddy Simulations can be dynamically informed by large-scale numerical weather prediction models, resulting in more accurate and reliable simulations of the planetary boundary layer. This approach has numerous beneficial applications, including the wind energy sector. It is a promising approach in fully understanding, managing, and predicting the performance of current and future wind farms, by advancing our understanding of atmospheric flow dynamics. Ultimately, this would contribute to a widespread efficient and affordable deployment of wind energy, thereby reducing reliance on fossil fuels and mitigating the impact of climate change. However, given the inherent complexity of expensive multiscale simulations, numerous assumptions and fine tuning is required to produce accurate output that is of practical importance. One key aspect of uncertainty is turbulence modeling across different resolutions, which is further complicated by the recently defined *gray zone* problem[13].For realistic problems, the selection of initial and boundary conditions and topography and land use datasets is also a potential source of uncertainty. The relative importance of such assumptions for wind energy applications is the main focus of the present study.

Specifically, we take advantage of a recent dataset of multiscale WRF simulations[42] to investigate the model sensitivity to different input factors and assumptions over the innermost, microscale domain, both in the temporal and in the spatial domain. Sensitivity analysis is used to identify key drivers of model behavior and guide future model development and improvement. The goal of our work is to complement the analysis of Giani and Crippa[42], by focusing on implications for wind energy. Meso- to micro-scale coupling techniques are still in their early stage and their application for wind power estimates has hardly

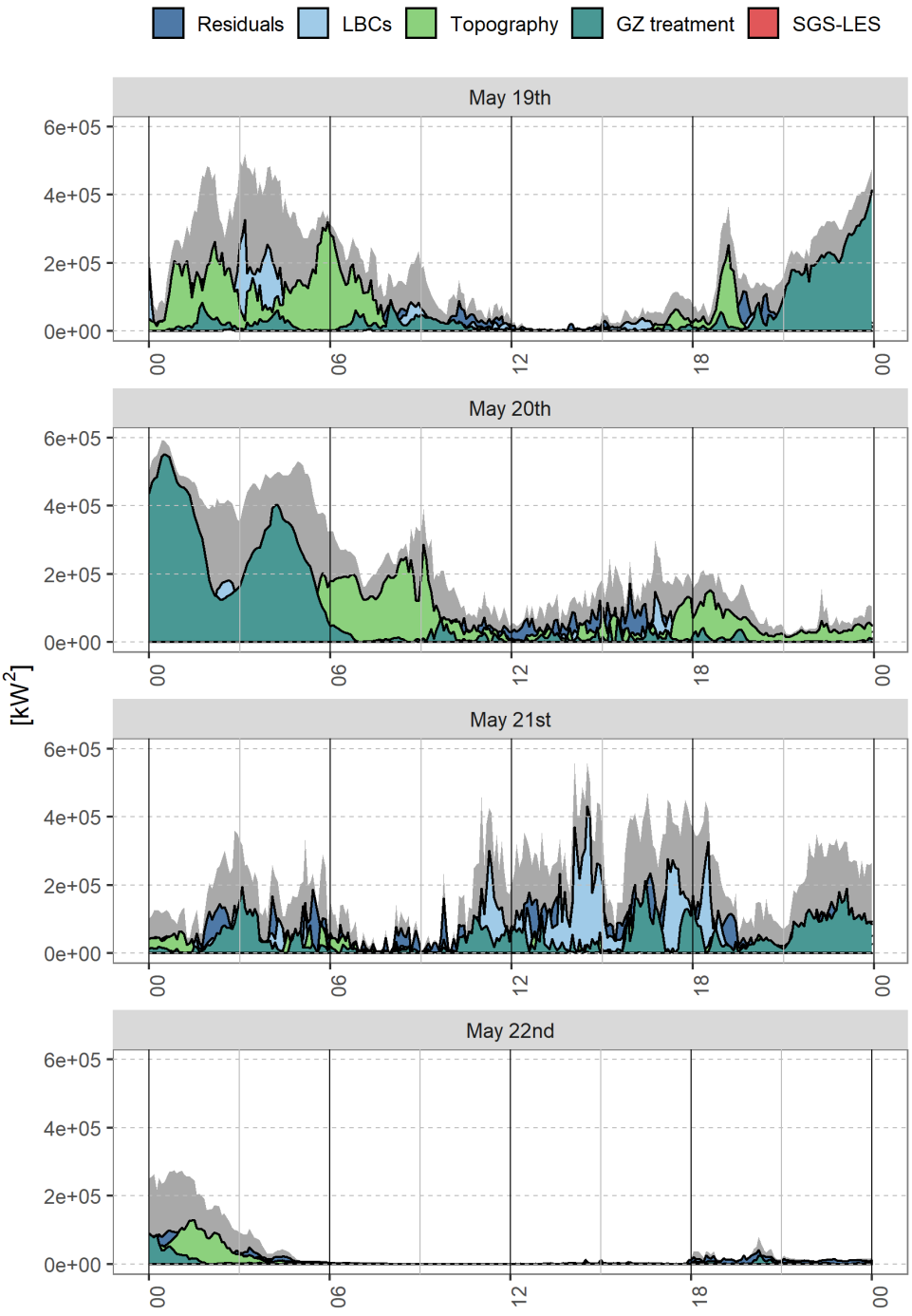

FIGURE 11 Decomposition of total variance [kW^2] of wind power at 78 m above ground at the turbine site on each simulated day. The total variance is reported in gray.

been explored and assessed, in particular in an area of complex terrain such as the Perdigão. The present study works in this direction, aiming to understand how different configurations of multiscale simulations impact wind energy predictions. To this end, several input assumptions are investigated through a four-way ANOVA of an ensemble of simulations conducted over an area of complex terrain in central Portugal during a four-day long, precipitation-free springtime period. Both time-averaged estimates and time-resolved series were investigated, of both wind speed at hub height and power productions. It is important

to acknowledge that our findings pertain specifically to our model setup at the Perdigão field site, for the four days considered. Nevertheless, they provide valuable insights into understanding the sensitivity of practical multiscale experiments conducted in complex terrain and shed light on the underlying mechanisms driving this sensitivity. Expanding this study to different geographical areas can be helpful in determining the applicability of our findings on a broader scale.

First, the analyses presented in this work show significant discrepancies in wind speed estimates with multiscale simulations, that lead to even more considerable variations in wind power calculations. In particular, this variability is stronger over the ridges and in the in-between valley. For a 2MW wind turbine located on the South-West ridge, we find that the ensemble average power production predicted by multiscale simulations is 840 kW for a four-day time average (capacity factor of 0.42), and that the interquartile range across the ensemble members is approximately 250 kW. In other words, the 75th percentile estimate predicts that up to approximately 850 standard American households (1.2 kW/household) could be powered by one single 2MW wind turbine, whereas the 25th percentile estimate predicts that about 625 households could be powered (assuming to perfectly match the load). When scaling up these findings for an entire wind farm, the variations among simulations can become significant for real-world wind energy challenges. While there is strong potential for multiscale simulations to fill in gaps in estimating wind energy resources, there is a need of targeting this uncertainty to make multiscale tools fully operational for wind energy purposes.

We further analyzed the main factors that explain such uncertainty in multiscale calculations, to inform future research directions. First, we find that most of the ensemble discrepancies occur during day-to-night transitions and synoptic transitions. Variance decomposition demonstrated that the resolution of topography and land use dataset are the primary factor of such variability. However, under specific periods of time (i.e., synoptic and day-night transitions) simulations are also sensitive to other factors, as mesoscale LBCs and modeling turbulence in the gray zone, which can locally overtake topography. The model appears insensitive to how the sub-grid scale is modeled in the innermost domain, somewhat differently from what found in idealized studies[61]. In other words, other factors relevant in realistic simulations appear to be more important than the SGS model in predicting hub-height wind speed with multiscale simulations. Furthermore, in the deepest region of the valley, only the topography factor drives differences within the ensemble, regardless of the sub-period analyzed.

Decomposition of variance performed on high-resolution temporal data (five-minutes) over the whole time series at the turbine site indicates strong inter-daily variability, and a coherent and recurrent daily pattern is not found. Occasionally, individual factors can persistently prevail over the others for certain time frames, in driving the overall ensemble spread. In summary, when conducting a time-averaged analysis for applications such as optimal turbine placement and studying regional climatology, special care should be taken in selecting appropriate topography and land use datasets, because they have a large effect on the long-term *time-averaged* wind speed. On the other hand, for short term forecasts of wind power, such as those one needed for energy market applications, it appears that the way that turbulence is modeled across scales can have significant impacts on the final wind power forecasts.

AUTHOR CONTRIBUTIONS

Conceptualization, PG, PC and GL; methodology, PG, PC and GD; software, GD and PG; validation, GD and PG; formal analysis, GD; investigation, PG and GD; resources, PC; data curation, GD and PG; writing—original draft preparation, GD, PC and PG; writing—review and editing, PG, PC, GD and GL; visualization, GD; supervision, GL and PC; project administration, GL and PC; funding acquisition, PC. All authors have read and agreed to the published version of the manuscript.

DATA AVAILABILITY STATEMENT

Time-resolved wind data for the 36 numerical simulations presented in this work are available at the following permanent repository (https://github.com/Env-an-Stat-group/23.DeMoliner.WE). Spatial data are available upon request.

FINANCIAL DISCLOSURE

This study is based upon work supported by the National Science Foundation under Grant No. 2236504 to PC.

CONFLICT OF INTEREST

The authors declare no conflict of interest.The funders had no role in the design of the study; in the collection, analyses, or interpretation of data; in the writing of the manuscript; or in the decision to publish the results.

References

1. European Commission . European Green Deal. https://ec.europa.eu/info/strategy/priorities-2019-2024/european-green-deal_en; 2020. Accessed: April 21, 2023.

2. International Energy Agency . *World Energy Outlook 2022*. OECD/IEA, 2022. Accessed: April 21, 2023.

3. National Development and Reform Commission of the Peoples Republic of China . Outline of the 14th Five-Year Plan (2021-2025) for National Economic and Social Development and the Long-Range Objectives Through the Year 2035. http://www.gov.cn/zhengce/2021-03/11/content_5591362.htm; 2021. Accessed: April 21, 2023.

4. Jacobson MZ, Delucchi MA. Providing all global energy with wind, water, and solar power, Part I: Technologies, energy resources, quantities and areas of infrastructure, and materials. *Energy Policy.* 2011;39(3):1154-1169. doi: https://doi.org/10.1016/j.enpol.2010.11.040

5. Jacobson MZ, Archer CL. Saturation wind power potential and its implications for wind energy. *Proceedings of the National Academy of Sciences.* 2012;109(39):15679-15684. doi: 10.1073/pnas.1208993109

6. Veers P, Dykes K, Lantz E, et al. Grand challenges in the science of wind energy. *Science.* 2019;366(6464). doi: 10.1126/science.aau2027

7. Dykes K, Hand M, Stehly T, et al. Enabling the SMART Wind Power Plant of the Future Through Science-Based Innovation. tech. rep., National Renewable Energy Laboratory; Golden, Colorado: 2017.

8. Haupt SE, Kosovic B, Shaw W, et al. On bridging a modeling scale gap: Mesoscale to microscale coupling for wind energy. *Bulletin of the American Meteorological Society.* 2019;100(12):2533–2550.

9. Lundquist KA, Chow FK, Lundquist JK. An immersed boundary method for the Weather Research and Forecasting model. *Monthly Weather Review.* 2010;138(3):796–817.

10. Jiménez-Esteve B, Udina M, Soler MR, Pepin N, Miró JR. Land use and topography influence in a complex terrain area: A high resolution mesoscale modelling study over the Eastern Pyrenees using the WRF model. *Atmospheric Research.* 2018;202(November 2017):49–62. doi: 10.1016/j.atmosres.2017.11.012

11. Giani P, Genton MG, Crippa P. Modeling the convective boundary layer in the Terra Incognita: Evaluation of different strategies with real-case simulations. *Monthly Weather Review.* 2022;150(5):981–1001.

12. Haupt SE, Berg LK, Churchfield M, Kosović B, Mirocha J, Shaw W. Mesoscale to Microscale Coupling for Wind Energy Applications: Addressing the Challenges. *Journal of Physics: Conference Series.* 2020. doi: 10.1088/1742-6596/1452/1/012076

13. Wyngaard JC. Toward numerical modeling in the Terra Incognita. *Journal of Atmospheric Sciences.* 2004;61(14):1816–1826.

14. Zhou B, Simon JS, Chow FK. The convective boundary layer in the terra incognita. *Journal of the Atmospheric Sciences.* 2014;71(7):2545–2563.

15. Rai RK, Berg LK, Kosovi B, et al. Evaluation of the Impact of Horizontal Grid Spacing in Terra Incognita on Coupled MesoscaleMicroscale Simulations Using the WRF Framework. *Monthly Weather Review.* 2019;147(3):1007 - 1027. doi: https://doi.org/10.1175/MWR-D-18-0282.1

16. Ching J, Rotunno R, LeMone M, et al. Convectively induced secondary circulations in fine-grid mesoscale numerical weather prediction models. *Monthly Weather Review.* 2014;142(9):3284–3302.

17. Mirocha JD, Churchfield MJ, Muñoz-Esparza D, et al. Large-eddy simulation sensitivities to variations of configuration and forcing parameters in canonical boundary-layer flows for wind energy applications. *Wind Energy Science.* 2018;3(2):589–613.

18. Liu Y, Liu Y, Muñoz-Esparza D, Hu F, Yan C, Miao S. Simulation of flow fields in complex terrain with WRF-LES: sensitivity assessment of different PBL treatments. *Journal of Applied Meteorology and Climatology.* 2020;59(9):1481–1501.

19. Muñoz-Esparza D, Kosovic B. Generation of inflow turbulence in large-eddy simulations of nonneutral atmospheric boundary layers with the cell perturbation method. *Monthly Weather Review.* 2018;146(6):1889–1909. doi: 10.1175/MWR-D-18-0077.1

20. Wise AS, Neher JMT, Arthur RS, Mirocha JD, Lundquist JK, Chow FK. Meso- to microscale modeling of atmospheric stability effects on wind turbine wake behavior in complex terrain. *Wind Energy Science.* 2022;7:367–386.

21. Volker PJ, Badger J, Hahmann AN, Ott S. The explicit wake parametrisation V1.0: A wind farm parametrisation in the mesoscale model WRF. *Geoscientific Model Development.* 2015;8(11):3715–3731. doi: 10.5194/gmd-8-3715-2015

22. Conry P, Sharma A, Potosnak MJ, et al. Chicagos heat island and climate change: Bridging the scales via dynamical downscaling. *Journal of Applied Meteorology and Climatology.* 2015;54(7):1430–1448.

23. Zhang X, Bao JW, Chen B, Grell ED. A three-dimensional scale-adaptive turbulent kinetic energy scheme in the WRF-ARW model. *Monthly Weather Review.* 2018;146(7):2023–2045.

24. Ito J, Niino H, Nakanishi M, Moeng CH. An extension of the MellorYamada model to the terra incognita zone for dry convective mixed layers in the free convection regime. *Boundary-layer meteorology.* 2015;157(1):23–43.

25. Boutle IA, Eyre JEJ, Lock AP. Seamless stratocumulus simulation across the turbulent gray zone. *Monthly Weather Review.* 2014;142(4):1655–1668.

26. Shin HH, Hong SY. Representation of the subgrid-scale turbulent transport in convective boundary layers at gray-zone resolutions. *Monthly Weather Review.* 2015;143(1):250–271.

27. Juliano TW, Kosović B, Jiménez PA, Eghdami M, Haupt SE, Martilli A. Gray Zone Simulations using a Three-Dimensional Planetary Boundary Layer Parameterization in the Weather Research and Forecasting Model. *Monthly Weather Review.* 2021;150(7):1585–1619. doi: 10.1175/mwr-d-21-0164.1

28. Talbot C, Bou-Zeid E, Smith J. Nested mesoscale large-eddy simulations with WRF: Performance in real test cases. *Journal of Hydrometeorology.* 2012;13(5):1421–1441.

29. Rai RK, Berg LK, Kosović B, Mirocha JD, Pekour MS, Shaw WJ. Comparison of measured and numerically simulated turbulence statistics in a convective boundary layer over complex terrain. *Boundary-Layer Meteorology.* 2017;163(1):69–89.

30. MuñozEsparza D, Lundquist JK, Sauer JA, Kosović B, Linn RR. Coupled mesoscaleLES modeling of a diurnal cycle during the CWEX13 field campaign: From weather to boundarylayer eddies. *Journal of Advances in Modeling Earth Systems.* 2017;9(3):1572–1594.

31. Doubrawa P, Muñoz-Esparza D. Simulating real atmospheric boundary layers at gray-zone resolutions: How do currently available turbulence parameterizations perform?. *Atmosphere.* 2020;11(4):345.

32. Dudhia J. Challenges in Sub-Kilometer Grid Modeling of the Convective Planetary Boundary Layer. *Meteorology.* 2022;1:402-413. doi: 10.3390/meteorology1040026

33. Giani P, Tagle F, Genton MG, Castruccio S, Crippa P. Closing the gap between wind energy targets and implementation for emerging countries. *Applied Energy.* 2020;269:115085.

34. Vanderwende BJ, Kosovic B, Lundquist JK, Mirocha JD. Simulating effects of a wind-turbine array using LES and RANS. *Journal of Advances in Modeling Earth Systems.* 2017:548–565. doi: 10.1002/2016MS000652.Received

35. Wang Q, Luo K, Yuan R, Wang S, Fan J, Cen K. A multiscale numerical framework coupled with control strategies for simulating a wind farm in complex terrain. *Energy.* 2020;203:117913. doi: 10.1016/j.energy.2020.117913

36. Arthur RS, Mirocha JD, Marjanovic N, et al. Multi-scale Simulation of Wind Farm Performance during a Frontal Passage. *Atmosphere.* 2020;11. doi: 10.3390/atmos11030245

37. Prósper MA, Otero-Casal C, Fernández FC, Miguez-Macho G. Wind power forecasting for a real onshore wind farm on complex terrain using WRF high resolution simulations. *Renewable Energy.* 2019;135:674–686. doi: 10.1016/j.renene.2018.12.047

38. Marjanovic N, Wharton S, Chow FK. Investigation of model parameters for high-resolution wind energy forecasting: Case studies over simple and complex terrain. *Journal of Wind Engineering and Industrial Aerodynamics.* 2014;134:10–24. doi: 10.1016/j.jweia.2014.08.007

39. Solbakken K, Birkelund Y. Evaluation of the Weather Research and Forecasting (WRF) model with respect to wind in complex terrain. *Journal of Physics: Conference Series.* 2018;1102. doi: 10.1088/1742-6596/1102/1/012011

40. Stieren A, Gadde SN, Stevens RJ. Modeling dynamic wind direction changes in large eddy simulations of wind farms. *Renewable Energy.* 2021;170:1342-1352. doi: 10.1016/j.renene.2021.02.018

41. Shi J, Liu Y, Li Y, et al. Wind Speed Forecasts of a Mesoscale Ensemble for Large-Scale Wind Farms in Northern China: Downscaling Effect of Global Model Forecasts. *Energies.* 2022;15. doi: 10.3390/en15030896

42. Giani P, Crippa P. On the Sensitivity of Large Eddy Simulations of the Atmospheric Boundary Layer Coupled with Realistic Large Scale Dynamics. *Under Review in Monthly Weather Review.* 2023.

43. Fernando HJ, Mann J, Palma JM, et al. The Perdigão: Peering into Microscale Details of Mountain Winds. *Bulletin of the American Meteorological Society.* 2019;100(5):799–820. doi: 10.1175/BAMS-D-17-0227.1

44. Wagner J, Gerz T, Wildmann N, Gramitzky K. Long-term simulation of the boundary layer flow over the double-ridge site during the Perdigão 2017 field campaign. *Atmospheric Chemistry and Physics.* 2019;19(2):1129–1146.

45. Quimbayo-Duarte J, Wagner J, Wildmann N, Gerz T, Schmidli J. Evaluation of a forest parameterization to improve boundary layer flow simulations over complex terrain. A case study. *Geoscientific Model Development.* 2022;15:5195–5209.

46. Connolly A, Veen vL, Neher J, Geurts BJ, Mirocha J, Chow FK. Efficacy of the cell perturbation method in large-eddy simulations of boundary layer flow over complex terrain. *Atmosphere.* 2021;12(1):1–28. doi: 10.3390/atmos12010055

47. Skamarock WC, Klemp JB, Dudhia JB, et al. A Description of the Advanced Research WRF Model Version 4.3. Tech. Rep. July, National Center for Atmospheric Research (NCAR); Boulder, Colorado: 2021.

48. Werner M. Shuttle Radar Topography Mission (SRTM) Mission Overview. *Frequenz.* 2001;55:75-79.

49. Pineda N, Jorba O, Jorge J, Baldasano JM. Using NOAA AVHRR and SPOT VGT data to estimate surface parameters: Application to a mesoscale meteorological model. *International Journal of Remote Sensing.* 2004;25(1):129–143. doi: 10.1080/0143116031000115201

50. NCEP . NCEP GDAS/FNL 0.25 Degree Global Tropospheric Analyses and Forecast Grids. Online Dataset; 2015

51. European Centre for Medium-Range Weather Forecasts . ECMWF's Operational Model Analysis, starting in 2011. Online Dataset; 2011.

52. Hersbach H, Bell B, Berrisford P, et al. The ERA5 global reanalysis. *Quarterly Journal of the Royal Meteorological Society.* 2020;146(730):1999–2049. doi: 10.1002/qj.3803

53. Hong SY, Noh Y, Dudhia J. A new vertical diffusion package with an explicit treatment of entrainment processes. *Monthly weather review.* 2006;134(9):2318–2341.

54. Deardorff JW. Stratocumulus-capped mixed layers derived from a three-dimensional model. *Boundary-Layer Meteorology.* 1980;18(4):495–527. doi: 10.1007/BF00119502

55. Smagorinsky J. General circulation experiments with the primitive equations: I. The basic experiment. *Monthly weather review.* 1963;91(3):99–164.

56. Lilly DK. The representation of small-scale turbulence in numerical simulation experiments. *IBM Form.* 1967:195–210.

57. Wilks DS. *Statistical methods in the atmospheric sciences*. Amsterdam; Boston: Elsevier Academic Press, 2011.

58. Pierrot M. The Wind Power Database. https://www.thewindpower.net/index.php; . Accessed: January, 2023.

59. Venkatraman K, Hågbo TO, Buckingham S, Giljarhus KET. Effect of different source terms and inflow direction in atmospheric boundary modeling over the complex terrain site of Perdigão. *Wind Energy Science.* 2023;8:85-108. doi: 10.5194/wes-8-85-2023

60. Simon JS, Chow FK. Alternative Anisotropic Formulations for Eddy-Viscosity Models in the Weather Research and Forecasting Model. *Boundary-Layer Meteorology.* 2021;181:11-37. doi: 10.1007/s10546-021-00642-0

61. Ma Y, Liu H. Large-Eddy Simulations of Atmospheric Flows Over Complex Terrain Using the Immersed-Boundary Method in the Weather Research and Forecasting Model. *Boundary-Layer Meteorology.* 2017;165(3):421–445. doi: 10.1007/s10546-017-0283-9

62. EIA . U.S. Energy Information Administration, Residential Energy Consumption Survey (RECS). Online Dataset; 2020.